The Astrophysical Journal Letters, 915:L13 (14pp), 2021 July 1 https://doi.org/10.3847/2041-8213/ac061f

Constraining the Primordial Lithium Abundance: New Cross Section Measurement of the ^{7}Be + n Reactions Updates the Total ^{7}Be Destruction Rate

S. Hayakawa[1], M. La Cognata[2], L. Lamia[2,3,4], H. Yamaguchi[1,5], D. Kahl[6,19], K. Abe[1], H. Shimizu[1], L. Yang[1,20], O. Beliuskina[1,21], S. M. Cha[7,22], K. Y. Chae[7], S. Cherubini[2,3], P. Figuera[2], Z. Ge[8,21], M. Gulino[2,9], J. Hu[10], A. Inoue[11], N. Iwasa[12], A. Kim[13], D. Kim[13,22], G. Kiss[8,23], S. Kubono[1,8,10], M. La Commara[14,15], M. Lattuada[2,3], E. J. Lee[7], J. Y. Moon[16], S. Palmerini[17,18], C. Parascandolo[15], S. Y. Park[13,24], V. H. Phong[8,25], D. Pierroutsakou[15], R. G. Pizzone[2], G. G. Rapisarda[2], S. Romano[2,3,4], C. Spitaleri[2,3], X. D. Tang[10], O. Trippella[17,18], A. Tumino[2,9], and N. T. Zhang[10]

[1] Center for Nuclear Study, University of Tokyo, RIKEN Campus, 2-1 Hirosawa, Wako, Saitama 351-0198, Japan; hayakawa@cns.s.u-tokyo.ac.jp
[2] Istituto Nazionale di Fisica Nucleare—Laboratori Nazionali del Sud, Via S. Sofia 62, I-95123 Catania, Italy
[3] Department of Physics and Astronomy "Ettore Majorana," University of Catania, Via S. Sofia 64, I-95123 Catania, Italy
[4] Centro Siciliano di Fisica Nucleare e Struttura della Materia, CSFNSM, Catania, Italy
[5] National Astronomical Observatory of Japan, Mitaka, 181-8588 Tokyo, Japan
[6] School of Physics and Astronomy, University of Edinburgh, J.C. Maxwell Bldg., P.G. Tait Rd., Edinburgh EH9 3FD, UK
[7] Department of Physics, Sungkyunkwan University, 2066, Seobu-ro, Jangan-gu, Suwon 16419, Republic of Korea
[8] RIKEN Nishina Center, 2-1 Hirosawa, Wako, Saitama 351-0198, Japan
[9] Faculty of Engineering and Architecture, Kore University of Enna, Cittadella Universitaria, I-94100 Enna, Italy
[10] Institute of Modern Physics, Chinese Academy of Sciences, Nanchang Road 509, Lanzhou 730000, People's Republic of China
[11] Research Center for Nuclear Physics, Osaka University, 10-1 Mihogaoka, Ibaraki, Osaka 567-0047, Japan
[12] Department of Physics, Tohoku University, 6-3 Aramaki-Aza-Aoba, Aoba, Sendai, Miyagi 980-8578, Japan
[13] Department of Physics, Ewha Womans University, 52, Ewhayeodae-gil, Seodaemun-gu, Seoul 03760, Republic of Korea
[14] Department of Physics 'E. Pancini', University of Naples Federico II, Complesso Universitario di Monte S. Angelo, Via Cintia, 21-80126 Naples, Italy
[15] Istituto Nazionale di Fisica Nucleare—Section of Naples, Complesso Universitario di Monte S. Angelo, ed. 6, Via Cintia, I-80126 Naples, Italy
[16] Rare Isotope Science Project, Institute for Basic Science, 70, Yuseong-daero 1689-gil, Yuseong-gu, Daejeon 305-811, Republic of Korea
[17] Istituto Nazionale di Fisica Nucleare—Section of Perugia, Via A. Pascoli, I-06123 Perugia, Italy
[18] Department of Physics and Geology, University of Perugia, Via A. Pascoli, I-06123 Perugia, Italy

Received 2021 March 22; revised 2021 May 14; accepted 2021 May 27; published 2021 July 1

Abstract

The cosmological lithium problem (CLP) stems from the outstanding discrepancy between theoretical predictions and astronomical observations of primordial lithium abundances. For the radiogenic production of ^{7}Li, ^{7}Be plays a pivotal role in the Big Bang nucleosynthesis (BBN). Nevertheless, the data for neutron-induced ^{7}Be destruction processes were still sparse, and especially lacked information on the contributions of transitions to the ^{7}Li excited states. In this work, we have determined the ^{7}Be(n, p_0)^{7}Li, ^{7}Be(n, p_1)^{7}Li*, and ^{7}Be(n, α)^{4}He reaction cross sections by means of the Trojan Horse method. The present and the previous data were analyzed together by a multichannel R-matrix fit, providing an improved uncertainty evaluation of the (n, p_0) channel and the first-ever quantification of the (n, p_1) contribution in the BBN-relevant energy range. We implemented the revised total reaction rate summing both the (n, p_0) and (n, p_1) contributions in a state-of-the-art BBN code PRIMAT. As a consequence, the present nuclear-physics data offers a reduction of the predicted ^{7}Li abundance by about one-tenth, which would impose a stricter constraint on BBN and head us in the correct direction to the CLP solution.

Unified Astronomy Thesaurus concepts: Big Bang nucleosynthesis (151); Nuclear reaction cross sections (2087); Nuclear abundances (1128)

1. Introduction

Big Bang nucleosynthesis (BBN; Cyburt et al. 2016; Coc & Vangioni 2017; Pitrou et al. 2018) is a critical probe to understand the early universe, describing the primordial production of light nuclides such as ^{4}He, D, ^{3}He, and ^{7}Li. The global agreement between the BBN predictions at the known baryon-to-photon number ratio (Ade et al. 2016; Pitrou et al. 2018) and the observations of galactic halo objects (Cyburt et al. 2016) is one of the few crucial pieces of evidence of the Big Bang. Nevertheless, the ^{7}Li/H abundance remains overestimated by a factor of 3–4, known as the cosmological lithium problem (CLP), which is still an open issue to be challenged by astronomy, nuclear physics, and nonstandard cosmology (Fields 2011). From the nuclear-physics point of view, the primordial radiogenic ^{7}Li abundance strongly depends on the ^{7}Be production and destruction process since ^{7}Li formed during BBN may easily be destroyed by the ^{7}Li (p, α)^{4}He reaction, while ^{7}Be will eventually decay into ^{7}Li

[19] Present address: Extreme Light Infrastructure–Nuclear Physics, Horia Hulubei National Institute for R&D in Physics and Nuclear Engineering (IFIN-HH), 077125 Bucharest-Măgurele, Romania.
[20] Present address: China Institute of Atomic Energy, P.O. Box 275(10), Beijing 102413, China.
[21] Present address: Department of Physics, University of Jyväskylä, P.O. Box 35, FI-40014 University of Jyväskylä, Finland.
[22] Present address: Center for Exotic Nuclear Studies, Institute for Basic Science, 55, Expo-ro, Doryong-dong, Yuseong-gu, Daejeon 34126, Republic of Korea.
[23] Present address: Institute for Nuclear Research (Atomki), H-4032 Debrecen, Bem ter 18/c, Hungary.
[24] Present address: Center for Underground Physics, Institute for Basic Science, 55, Expo-ro, Doryong-dong, Yuseong-gu, Daejeon 34126, Republic of Korea.
[25] Present address: Faculty of Physics, VNU University of Science, 334 Nguyen Trai, Thanh Xuan, 120062 Hanoi, Vietnam.

via the electron capture after BBN ends. A nuclear-physics solution to the CLP is, however, considered to have little hope (Coc & Vangioni 2017)—as long as the relevant nuclear data are valid.

There is indeed a new discovery by Damone et al. (2018) that a direct measurement of the main ^{7}Be destruction process ^{7}Be(n, p)^{7}Li with a wide-spectrum neutron beam revised the cross sections upward from the previous direct data by Koehler et al. (1988), which were widely used in BBN calculations, and thus led the ^{7}Li/H value downward. Another direct measurement by Tomandl et al. (2019) was performed only with a thermal neutron beam but achieved higher precision than Damone et al. (2018), providing an intermediate cross section value between the two previous studies (Damone et al. 2018; Koehler et al. 1988). Tomandl et al. (2019) also determined the cross section ratio σ_1/σ_0 of the transitions to the first excited state ^{7}Be(n, p_1)^{7}Li* and to the ground state ^{7}Be(n, p_0)^{7}Li to be 1.2% ± 0.6%, which is consistent with the value from Koehler et al. (1988). Contrarily, Damone et al. (2018) did not report any (n, p_1) yield, apparently because the proton kinetic energies of the (n, p_1) channel were too low to observe this channel with their ΔE-E silicon telescope (Barbagallo et al. 2018). de Souza et al. (2020) compiled the available ^{7}Be(n, p)^{7}Li data by a hierarchical Bayesian model, and an R-matrix fit derived a reaction rate with an evaluated uncertainty (∼2%) that is much smaller than the discrepancy among the different data sets (∼30%) they adopted. However, the contribution of the (n, p_1) channel was not taken into account in their R-matrix analysis since there were no (n, p_1) data available except at the thermal neutron energy. Therefore, the σ_1/σ_0 ratio at the BBN energies was still unknown, which will be quantitatively evaluated in this Letter.

Another important neutron-induced reaction, ^{7}Be(n, α)^{4}He, has contained large uncertainties until recently, but there have been also several experiments and reevaluations. These studies rely on some hypothesis or partial measurements, namely, the charge symmetry hypothesis (Hou et al. 2015; Lamia et al. 2017), the measurement of the ^{7}Be(n,$\gamma\alpha$) decays from limited excited states (Barbagallo et al. 2016), or the time-reversal reaction measurement at higher energies (Kawabata et al. 2017). Thus the data quality at the BBN energies is expected to be improved upon. The latest measurement by Lamia et al. (2019) performed at the EXOTIC radioactive-ion (RI) beam separator (Farinon et al. 2008) of Istituto Nazionale di Fisica Nucleare—Laboratori Nazionali di Legnaro serves as the basis of the present work with a common experimental technique, covering the BBN energies yet with limited statistics.

Therefore, we aimed at further validation of both reactions at the relevant energies that still have disagreements or large uncertainties for more precise BBN investigations.

2. Method

Our basic idea is to avoid experimental difficulties in direct use of a ^{7}Be target and a neutron beam by means of the Trojan Horse Method (THM; see Baur 1986; Tribble et al. 2014; Spitaleri et al. 2016 for general and practical instructions). THM has been known for its accessibility to a two-body reaction at astrophysical thermonuclear energies via a two-to-three-body reaction in a quasi-free (QF) kinematics condition. In practice, the triple differential cross section of the QF reaction is measured that is proportional to the half-off-energy-shell (HOES) differential cross section of the two-body process, and corrections by a proper penetration factor and normalization may deduce the on-energy-shell (OES) cross section of interest. This principle is applicable to reactions induced not only by charged particles but also by neutrons (Gulino et al. 2010, 2013) and with RI beams (Cherubini et al. 2015; Pizzone et al. 2016), as the former work (Lamia et al. 2019) mentioned above established the ^{7}Be(n, α)^{4}He reaction measurement via ^{2}H(^{7}Be, $\alpha\alpha$)^{1}H.

3. Experiment

The present experimental setup has an expanded capability to detect ^{7}Li recoils, enabling the ^{7}Be(n, p)^{7}Li reaction measurement via ^{2}H(^{7}Be,^{7}Lip)^{1}H. We employed a 64 μg cm^{-2} thick deuterated polyethylene (CD_2) target irradiated by a ^{7}Be RI beam at 3.16 MeV nucleon^{-1} with a typical intensity of 1×10^6 pps produced by Center-for-Nuclear-Study RI Beam separator (CRIB; Kubono et al. 2002; Yanagisawa et al. 2005; Yamaguchi et al. 2020) of the University of Tokyo, located at the RI Beam Factory, RIKEN. Two parallel plate avalanche counters (PPACs; Kumagai et al. 2001) installed in front of the target enabled event-by-event beam tracking. We mounted six ΔE-E silicon telescopes having charge-division position-sensitive detectors with 45 × 45 mm^2 active areas, surrounding the target at distances of 20 cm symmetrically to the beam axis at forward angles ±12°, ±34° and ±56°. The telescopes at ±34° and ±56° with 300 μm thick ΔE layers were optimized for light-particle detection (p and α), while the ones at ±12° with 20 μm thick ΔE layers newly enabled the heavy ion ^{7}Li identification from the scattered ^{7}Be. The coincidence measurement well suppressed the background events, which were checked with a CH_2 target. The present setup improved the angular and energy resolutions from those in Lamia et al. (2019) thanks to using the PPACs, the thinner CD_2 target, and finer position resolutions of the silicon detectors. The typical center-of-mass energy resolutions for the ^{7}Be(n, p)^{7}Li and the ^{7}Be(n, α)^{4}He reaction channels were estimated to be 50 keV and 180 keV, respectively.

4. Results

The reconstructed three-body Q-value spectra (Costanzo et al. 1990) from the observed coincidences ^{7}Li-p and α-α were consistent with the known Q values of the ^{7}Be(d,^{7}Lip_0)^{1}H (−0.580 MeV), ^{7}Be(d,^{7}Li$^*p_1$)^{1}H (−1.058 MeV), and ^{7}Be(d, $\alpha\alpha$)^{1}H (16.766 MeV) channels (Wang et al. 2017). Figure 1(a) shows the three-body Q-value distribution from the ^{7}Li-p observation versus their relative energy $E_{^7\mathrm{Li}\text{-}p}$. The experimental distribution (black dots) and the Monte Carlo simulations based on the experimental resolutions (red and blue crosses) have a fairly good agreement in the Q-value peak energies (red and blue dashed lines) as well as their broadenings. This is more clearly recognized in Figure 1(b), a projection of the data in Figure 1(a) to the Q-value axis, fitted by two overlapping Gaussian functions and their sum with peaks and widths representing the experimental dependency on $E_{^7\mathrm{Li}\text{-}p}$. In practice, such a fit process was applied at each $E_{^7\mathrm{Li}\text{-}p}$ bin with the Q-value peak positions and widths determined from the experimental data themselves of which $E_{^7\mathrm{Li}\text{-}p}$ dependency was confirmed by the simulation, then we extracted $E_{^7\mathrm{Li}\text{-}p}$ excitation functions separately for p_0 and p_1 as shown in Figure 1(c). A more quantitative discussion on validity of the "$p_0 + p_1$" model is given in Appendix A. The horizontal arrows in Figure 1(c)

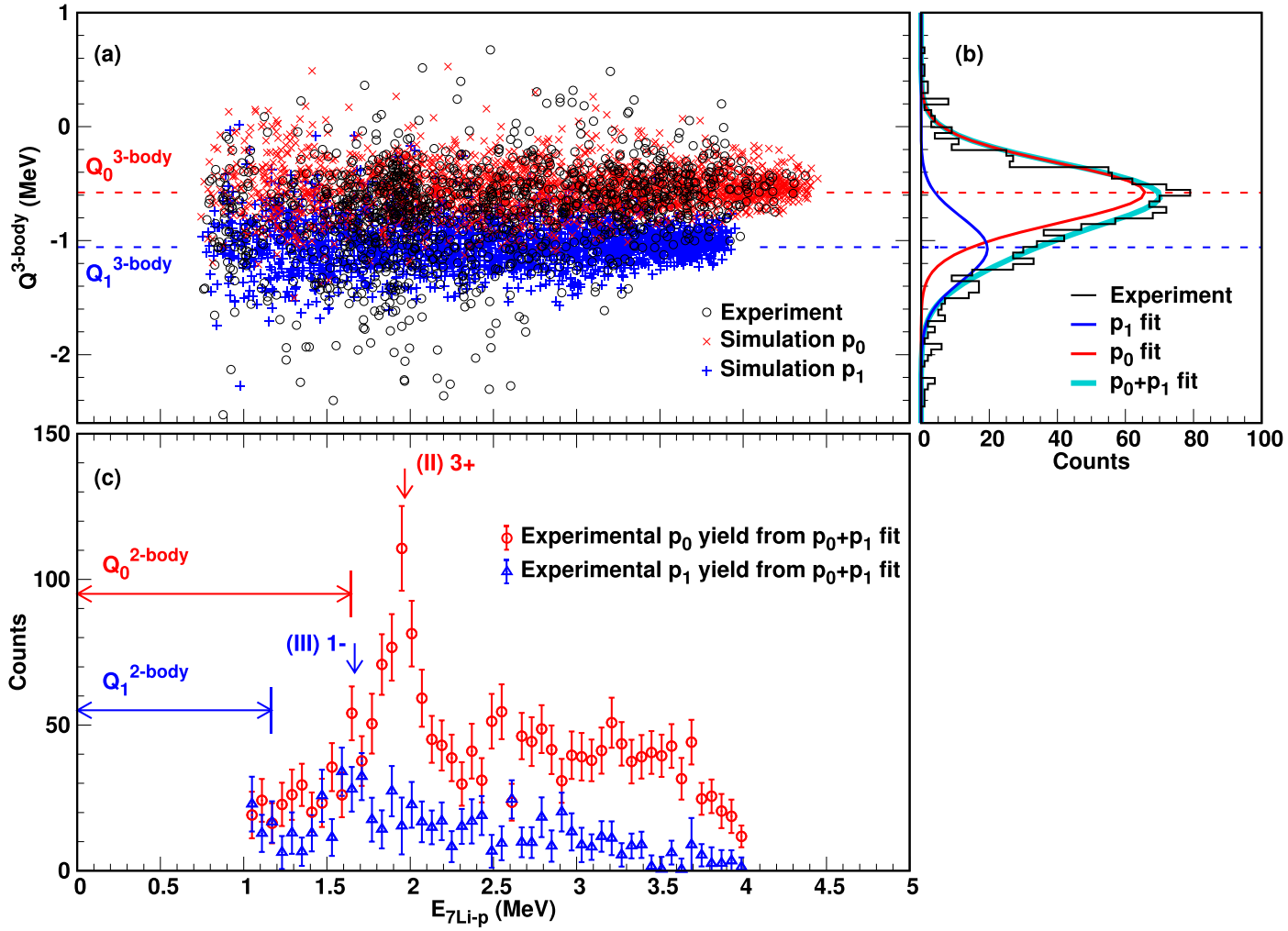

Figure 1. (a) ^{2}H(^{7}Be,^{7}Lip)^{1}H-channel Q value vs. ^{7}Li-p relative energy of the THM data and of the Monte Carlo simulation. (b) Projection of the data in (a) to the Q-value axis. (c) Excitation functions of the p_0 and p_1 channels determined by the summed-Gaussian fit.

represent the Q values of the two-body reactions ^{7}Be(n, p_0)^{7}Li and ^{7}Be(n, p_1)^{7}Li*, corresponding to the onset of center-of-mass energy defined by $E_{\text{c.m.}} \equiv E_{^7\text{Li-}p} - Q_{2\text{-body}}$. The vertical arrows in Figure 1(c) indicate characteristic resonances to be discussed later.

We confirmed the predominance of the QF mechanism by analyzing the shape of the observed p-n momentum distributions for both three-body reaction channels. From their consistency with the analytical Hulthén wave functions for deuteron, we selected the data below 60 MeV c^{-1} as true QF events for the further analysis. We assumed the differential cross section is isotropic owing to the limited statistics and angular coverage. Compared to the calculated angular distribution with the resonance parameters (see Section 5), we estimated the associated uncertainties as 10% and 40% for the ^{7}Be(n, p) and ^{7}Be(n, α) channels, respectively. The obtained HOES cross sections were corrected with the most dominant partial waves in the relevant energy ranges. As is clearer in Section 5, the ^{7}Be(n, p_0) excitation function in the relevant energy range is mainly characterized by the s- and p-wave resonances, but the latter is dominant only for a few data points around its sharp peak (3^+, $E_{\text{c.m.}} = 330$ keV) over the gentle tail of the former (2^-, $E_{\text{c.m.}} = 10$ keV). This allowed us s-wave-only correction, and normalization to the 330 keV peak of the previous data (Sekharan et al. 1976) despite of its p wave. The (n, p_1) channel is also considered s-wave dominant (1^-, $E_{\text{c.m.}} = 500$ keV), and we applied the same normalization factor as ^{7}Be(n, p_0) since our σ_1/σ_0 was determined from the yields shown in Figure 1(c). The ^{7}Be(n, α) channel is purely p-wave dominant, and normalized to the $E_{\text{c.m.}} = 1$ MeV peak (Hou et al. 2015; Kawabata et al. 2017; Lamia et al. 2017, 2019). The normalized cross sections multiplied by $\sqrt{E_{\text{c.m.}}}$ of the ^{7}Be(n, p_0)^{7}Li, ^{7}Be(n, p_1)^{7}Li*, and ^{7}Be(n, α)^{4}He reaction channels are shown in Figure 2. Note that their error bars include the statistical uncertainties, the normalization uncertainties, and the ones arising from the isotropic approximation, added in quadrature. We also plotted the previous data and evaluations for comparison (Borchers & Poppe 1963; Poppe et al. 1976; Sekharan et al. 1976; Koehler et al. 1988; Hou et al. 2015; Barbagallo et al. 2016; Kawabata et al. 2017; Lamia et al. 2017, 2019; Damone et al. 2018; Tomandl et al. 2019) with labels defined in the caption of Figure 2. Note that the (n, p_1) cross sections obtained from the σ_1/σ_0 ratio by Koe88 (Koehler et al. 1988) are renormalized to the Dam18 (n, p_0) cross sections (labeled as p_1/p_0 Koe88 $\times$ p_0 Dam18).

5. R-matrix Analysis

To obtain reaction rates in a wide temperature range $T_9 = 0.001$–10 (where T_9 is in units of 10^9 K) for BBN

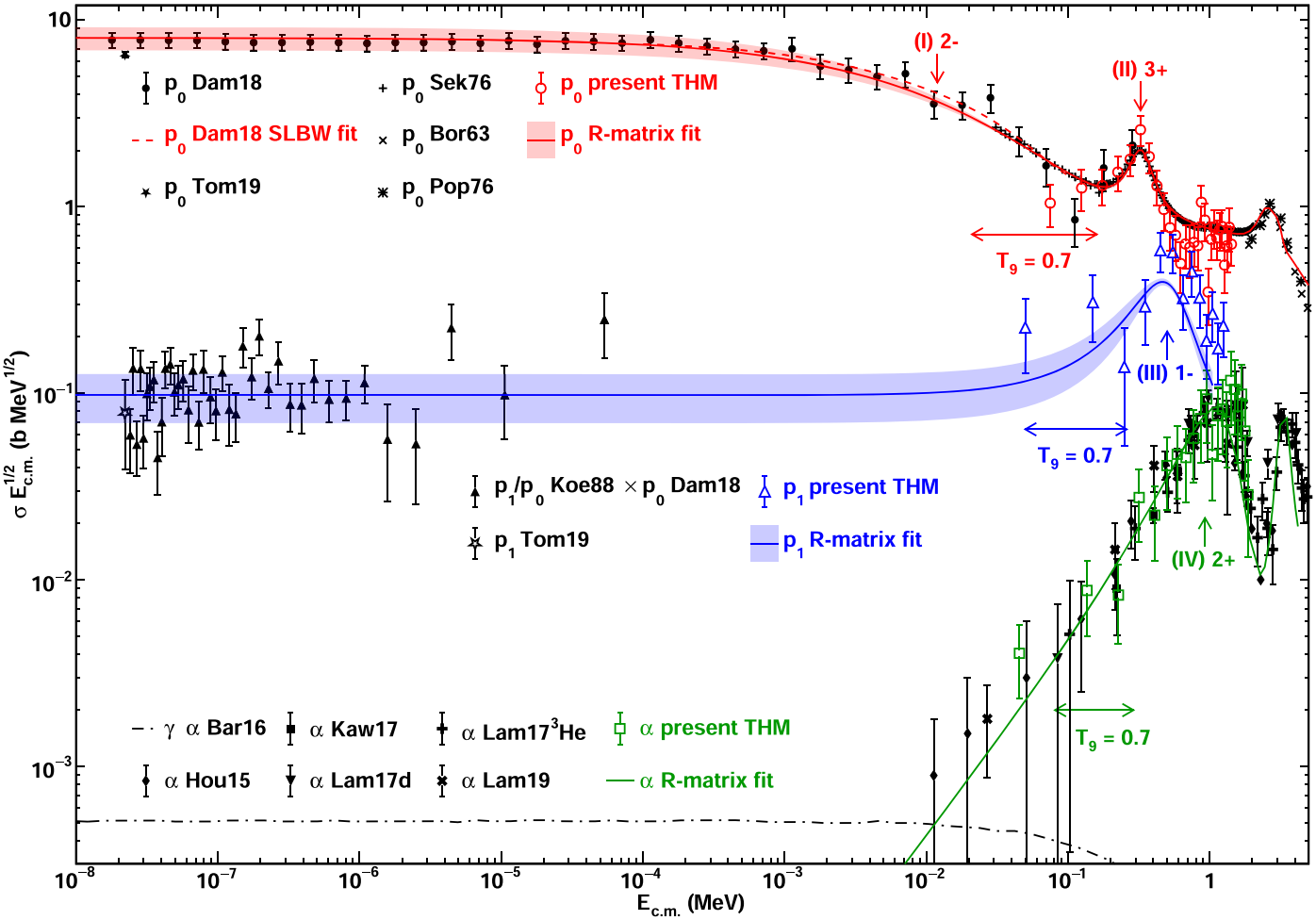

Figure 2. The present cross sections multiplied by $\sqrt{E_{\rm c.m.}}$ of the ^{7}Be(n, p_0)^{7}Li, the ^{7}Be(n, p_1)^{7}Li*, and the ^{7}Be(n, α)^{4}He reactions are shown as open red circles, blue triangles, and green squares, respectively. The previous experimental data and evaluations are labeled as Dam18 (Damone et al. 2018), Tom19 (Tomandl et al. 2019), Sek76 (Sekharan et al. 1976), Bor63 (Borchers & Poppe 1963), and Pop76 (Poppe et al. 1976) for (n, p_0); Koe88 (Koehler et al. 1988) and Tom19 for (n, p_1); Bar16 (Barbagallo et al. 2016) for (n, $\gamma\alpha$); and Hou15 (Hou et al. 2015), Kaw17 (Kawabata et al. 2017), Lam17d, Lam17^{3}He (Lamia et al. 2017), and Lam19 (Lamia et al. 2019) for (n, α). The solid lines are the present R-matrix fits with light-colored bands as their uncertainties.

calculation inputs, continuous excitation functions over 10^{-8} to a few MeV are needed for numerical integration. Therefore we performed an R-matrix analysis to compile both the present and the previous data of these three reaction channels by using AZURE2 (Azuma et al. 2010) including all the relevant partial widths Γ_n, Γ_{p0}, Γ_{p1}, and Γ_α. The ^{7}Be(n, p_0) data set used for the R-matrix analysis is based on the same selection as used in Damone et al. (2018), Damone (2018; part of Dam18 + Sek76 as displayed in Figure 2), and the present THM data, Bor63, and Pop76 are added. For the ^{7}Be(n, p_1) and ^{7}Be(n, α) channels, all the labeled data shown in Figure 2 (except for p_1 Tom19 and $\gamma\alpha$ Bar16) were used without any data cutoff. Appendix B shows the adopted data sets more explicitly. We included nine known levels below the ^{8}Be excitation energy of $E_x = 24$ MeV (Tilley et al. 2004) and an additional non-resonant background pole, with a common channel radius of 5 fm for each channel in the same manner as Adahchour & Descouvemont (2003). The most significant channel ^{7}Be (n, p_0)^{7}Li is dominated by four of these levels as described in detail by a former R-matrix study (Adahchour & Descouvemont 2003; Descouvemont et al. 2004); the 2^- resonance near the neutron threshold (labeled as level I) principally dominates the cross section up to the BBN energies, the two 3^+ states at $E_x = 19.24$ MeV (level II) and $E_x = 21.5$ MeV well characterize the corresponding single peaks, and a 2^+ background pole accounts for the enhancement at high energies. The most important resonances to expand analysis to the ^{7}Be(n, p_1)^{7}Li* and ^{7}Be(n, α)^{4}He channels are the 1^- state at $E_x = 19.4$ MeV (level III) and the 2^+ state at $E_x = 20.1$ MeV (level IV), respectively; the former expresses the ^{7}Be(n, p_1) resonance behavior peaked at $E_{\rm c.m.} \sim 0.5$ MeV tailing down to the thermal neutron energy by the $1/v$ law, and the latter forms the first peak in the ^{7}Be(n, α) spectrum around $E_{\rm c.m.} \sim 1$ MeV. Despite its importance in the (n, α) channel, level IV is much less significant in the total cross section especially at lower energies due to its p-wave nature. Therefore we imposed some restrictions on level IV, which made the analysis much simpler; fixing Γ_{p0}, Γ_{p1}, and Γ_α at a known ratio $\Gamma_\alpha/\Gamma_p \sim 4.5$ (Tilley et al. 2004), and freeing Γ_n and resonance energy (refitted to be 19.87 MeV) not to significantly exceed the known total width $\Gamma = 880$ keV (Tilley et al. 2004). The other four higher-lying levels (0^+ at $E_x = 20.2$ MeV, 2^+ at $E_x = 22.24$ MeV, 1^- at $E_x = 22$ MeV, and 2^- at $E_x = 24$ MeV) play rather supplementary roles mainly for the higher-energy behavior. The 4^+ and 4^- higher-spin states (at $E_x = 19.86$ MeV and 20.9 MeV, respectively) were not included due to their limited influences.

Table 1
Low-lying Resonance Parameters Resulted from the *R*-matrix Fit

Level No.	J^{π}	E_x	$E_{\rm c.m.}$	l_n	Γ_n	l_{p0}	Γ_{p0}	l_{p1}	Γ_{p1}	l_α	Γ_α	Γ	$\Gamma^{\rm (Ref.)}$
I	2^-	18910[a]	10	0	$297\ ^{+23}_{-32}$	0	$651\ ^{+55}_{-73}$	2	$\sim$0	⋯	⋯	$948\ ^{+59}_{-80}$	1634[b]
II	3^+	19230[b]	330	1	$89\ ^{+8}_{-9}$	1	$66\ ^{+4}_{-3}$	3	$\sim$0	⋯	⋯	$155\ ^{+9}_{-10}$	165[b]
III	1^-	19400[a]	500	0	$263\ ^{+56}_{-46}$	0	$\sim$0	0	$326\ ^{+75}_{-70}$	⋯	⋯	$589\ ^{+94}_{-84}$	645[a]
IV	2^+	$(19885\ ^{\pm 20})$	$(985\ ^{\pm 20})$	1	$(89\ ^{\pm 3})$	1	23[c]	1	143[c]	2	726[c]	(981)	880[a]

Notes. The brackets indicate provisional fit values. Energies are all in units of keV.
[a] From Tilley et al. (2004).
[b] From Adahchour & Descouvemont (2003).
[c] The proton and α widths of Level IV are fixed at a ratio $\Gamma_\alpha/\Gamma_p \sim 4.5$ (Tilley et al. 2004).

We do not introduce the γ-emission channels to fit the Bar16 plots (representing the ^{7}Be(n, $\gamma\alpha$)^{4}He reaction channel Barbagallo et al. 2016), which appears significant only below the BBN energies. See Appendix C for more details on the present *R*-matrix analysis.

The resulting resonance parameters of levels I–IV are listed in Table 1. The resonance energies and partial widths with uncertainty indices are the ones obtained by the present analysis. The initial partial widths of level I conform to that of Adahchour & Descouvemont (2003) and refitted to the present (n, p_0) data set, thus the Γ_n and Γ_{p0} were consequently larger than those evaluated in Koehler et al. (1988) and Tilley et al. (2004). The fixed level IV widths are indicated with double daggers, and the brackets specify provisional fitting results. The total Γ of levels I–IV is compared with the known values $\Gamma^{\rm (Ref.)}$ as in the rightmost column of Table 1. The fitted curves to the (n, p_0)-, (n, p_1)-, and (n, α)-channel cross sections appear as solid curves in Figure 2, associating their uncertainties in light-colored bands except for the (n, α)-channel due to the limited parameter freedom of level IV. The vertical arrows with the spin-parity indices in Figure 2 are placed at the resonance energies of levels I–IV, and the horizontal arrows indicate energy ranges so as to cover 68% of reaction rates for each reaction channel at a typical BBN temperature $T_9 = 0.7$. Note that our ^{7}Be(n, p_0) fitting curve appears significantly lower than that of the single-level Breit–Wigner fit by Damone et al. (2018; red dashed curve, p_0 Dam18 SLBW fit in Figure 2), especially around $E_{\rm c.m.} \sim 10$ keV (see Appendix D), where the *R*-matrix analysis does not demand resonances other than level I. Contrarily, Dam18 SLBW analysis attempted to best fit the experimental data (although their uncertainties are relatively large around $E_{\rm c.m.} \sim 10$ keV) assuming known resonances but without any constraints on partial widths, which let level-III Γ_n significantly exceed the Wigner limit (see Damone 2018).

6. Application to BBN

The uncertainties of the excitation functions from the *R*-matrix fitting (as shown in Figure 2) and those of the reaction rates were evaluated by a Monte Carlo simulation varying the resonance parameters around the best-fit values by their uncertainties. Figures 3(a)–(d) show the ^{7}Be(n, p)^{7}Li reaction rates with uncertainties relative to that of Cyburt (2004; black solid curve, Cyb04) in the same manner as Damone et al. (2018). The effective BBN temperature range of $T_9 = 0.23$–1.4 is indicated by cyan vertical bands. Figure 3(a) represents the previous ^{7}Be(n, p_0) rates DAACV04 (Descouvemont et al. 2004) and Dam18 (Damone et al. 2018), and the latter is plotted in each panel for comparison. One can see that the present p_0 rate in Figure 3(b) appears significantly lower than Dam18 p_0 as expected. Our recommended $p_0 + p_1$ rate in Figure 3(c) is ultimately comparable to Dam18 p_0 in the BBN range, but with different temperature dependence due to the (n, p_1) contribution. The sum of Dam18 p_0 and the present p_1 in Figure 3(d) represents a possible upper limit deducible from the adopted cross section data set, but the Dam18 p_0 contribution retains the large uncertainties. The present recommended reaction rate data sets and the analytic form are posted in Appendix E.

We have calculated the ^{7}Li/H abundances with the above ^{7}Be(n, p)^{7}Li reaction rates by using one of the most recent BBN codes PRIMAT (Pitrou et al. 2018, see Appendix F). Note that the present ^{7}Be(n, α)^{4}He reaction rate was found to offer little change ($\sim$0.1%) to the ^{7}Li/H yield compared to Bar16 rate (Barbagallo et al. 2016), which is used in PRIMAT by default, thus not to be discussed here. Table 2 compares the ^{7}Li/H yields (in units of 10^{-10}) at the baryon-to-photon number density ratio $\eta = 6.09 \times 10^{-10}$ (Pitrou et al. 2018) determined from the cosmic microwave background observation. The upper four rows demonstrate that the PRIMAT results with Cyb04 and Dam18 rates are consistent with those from Damone et al. (2018) who used the AlterBBN code (Arbey 2012) within the errors, although the PRIMAT ones tend to be slightly smaller. The lower four rows represent the comparison between the PRIMAT default rate (DAACV04) and the present ones. We highlight that the recommended $p_0 + p_1$ rate yields a significantly smaller ^{7}Li/H value ($5.18^{+0.22}_{-0.25} \times 10^{-10}$) than DAACV04 p_0 ($5.63^{+0.22}_{-0.24} \times 10^{-10}$) by about one-tenth or 2 standard deviations. The maximum possible rate Dam18 p_0 + present p_1 would derive an extra few percent reduction of ^{7}Li/H but rather retain the largest uncertainties in Table 2. Therefore, the recommended rate may impose a more strict constraint on the primordial ^{7}Li/H abundance owing to the reevaluation of the (n, p_0) uncertainty and the first-ever quantified (n, p_1) contribution, which should be adopted in future BBN investigations although we obviously need additional contributions to get closer to the observed ^{7}Li/H value $1.58 \pm 0.3 \times 10^{-10}$ (Sbordone et al. 2010).

7. Summary

We discussed the neutron-induced reactions on ^{7}Be, which play pivotal roles in the ^{7}Li production during BBN. We applied THM to measure the ^{7}Be(n, p)^{7}Li and the ^{7}Be(n, α)^{4}He reactions simultaneously via the ^{2}H(^{7}Be,^{7}Lip)^{1}H and the ^{2}H(^{7}Be, $\alpha\alpha$)^{1}H reactions with a ^{7}Be RI beam at CRIB. The multichannel *R*-matrix analysis with AZURE2 fitted both the previous and the present data consistently with the ^{8}Be

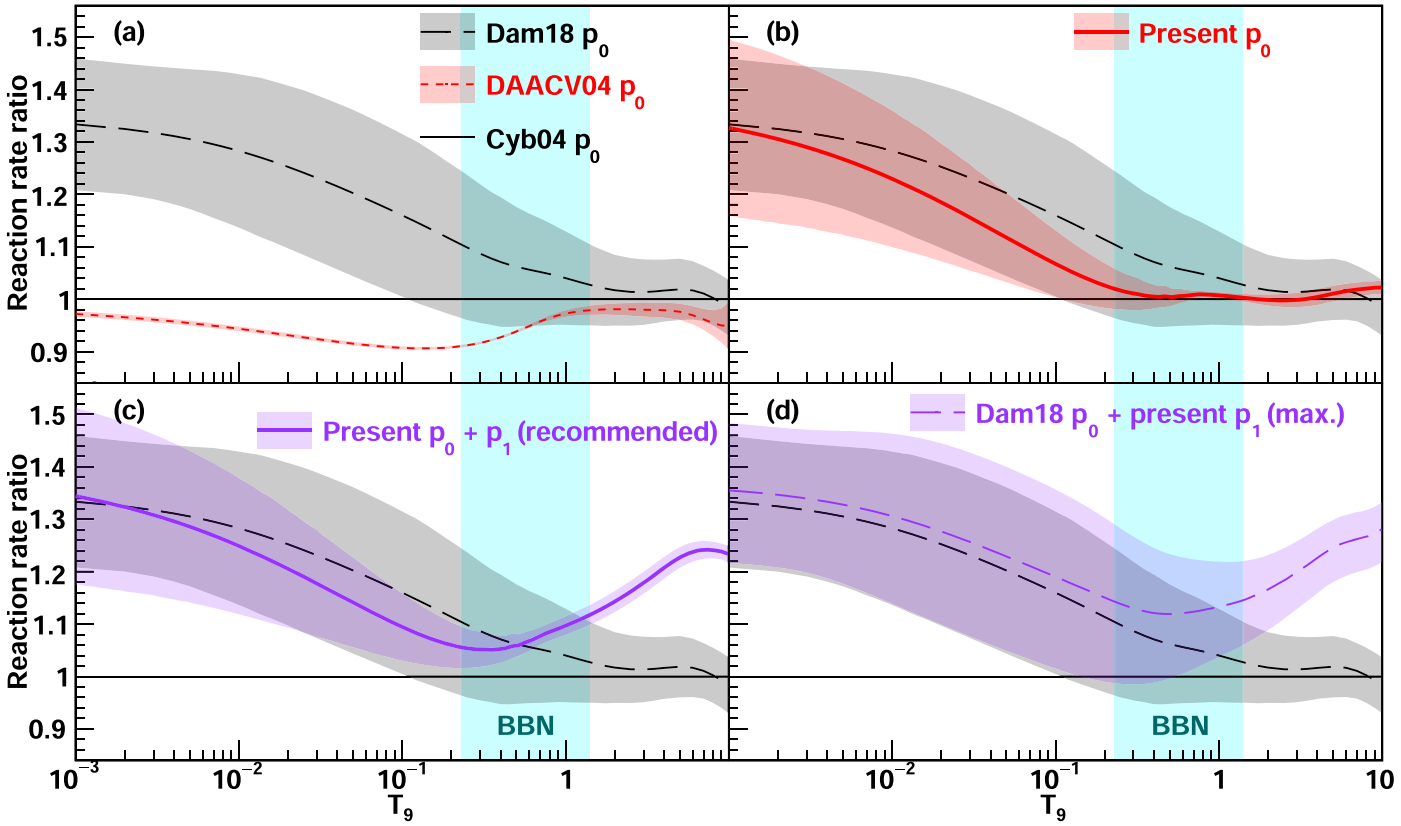

Figure 3. Comparison of the previous (Dam18, Damone et al. 2018; DAACV04, Descouvemont et al. 2004) and the present ^{7}Be(n, p)^{7}Li reaction rates relative to that of Cyb04 (Cyburt 2004) together with uncertainties in light-colored bands.

Table 2
^{7}Li Abundances at $\eta = 6.09 \times 10^{-10}$ (Pitrou et al. 2018) with Different BBN Calculation Codes and the ^{7}Be(n, p)^{7}Li Reaction Rate Sources

Reaction Rate Source	BBN Code	^{7}Li/H (10^{-10})
Cyb04 p_0 [a]	AlterBBN	5.46[b]
Dam18 p_0 [b]	AlterBBN	$5.26^{\pm 0.40}$[b]
Cyb04 p_0[a]	PRIMAT	$5.38^{+0.30}_{-0.31}$
Dam18 p_0[b]	PRIMAT	$5.15^{+0.43}_{-0.49}$
DAACV04 p_0 [c]	PRIMAT	$5.63^{+0.22}_{-0.24}$ [d]
Present p_0	PRIMAT	$5.37^{+0.22}_{-0.25}$
Present $p_0 + p_1$ (recommended)	PRIMAT	$5.18^{+0.22}_{-0.25}$
Dam18 p_0[b] + present p_1 (max.)	PRIMAT	$4.97^{+0.47}_{-0.41}$
Observation	...	$1.58^{\pm 0.3}$[e]

Notes.
[a] Cyburt (2004).
[b] Damone et al. (2018).
[c] Adahchour & Descouvemont (2003); Descouvemont et al. (2004).
[d] Pitrou et al. (2018).
[e] Sbordone et al. (2010).

resonance structure, which indicated slightly smaller ^{7}Be (n, p_0)^{7}Li cross sections with better uncertainty evaluations than those of Damone et al. (2018), and quantified the ^{7}Be (n, p_1)^{7}Li* contribution in the BBN energy range for the first time. The new BBN calculation by PRIMAT with the recommended $p_0 + p_1$ reaction rate substituting the default rate (Descouvemont et al. 2004) results in the decrement of the primordial ^{7}Li abundance by about one-tenth or 2 standard deviations, which is still incomplete but should be accounted for as a part of the solution to the CLP.

This experiment was performed at RI Beam Factory operated by RIKEN Nishina Center and CNS, University of Tokyo. This work was supported by JSPS KAKENHI (grant Nos. 15K17631, 18K13556, and 19K03883). K.Y.C. and S.M.C. were supported by National Research Foundation of Korea (Nos.2020R1I1A1A01065120,2020R1A2C1005981,2019K2-A9A2A10018827, and 2016R1A5A1013277). D. Kahl would like to thank the UK STFC for support. D. Kim acknowledges the support from the IBS grant funded by the Korean government (No. IBS-R031-D1). G.G.K. acknowledges the support by NKFIH (NN128072) and from the Janos Bolyai research fellowship of the Hungarian Academy of Sciences and from UNKP-20-5-DE-2 New National Excellence Program of the Ministry of Human Capacities of Hungary. The authors acknowledge Finanziamenti di Linea 2 and Starting Grant 2020 by University of Catania. We would like to give a special thanks to C. Pitrou and A. Coc for the helpful discussion about the PRIMAT calculation.

Software: AZURE2 (Azuma et al. 2010), PRIMAT (Pitrou et al. 2018).

Appendix A
Validity Test of the Extraction of the p_0- and p_1-channel Yields

We add a supplemental Figure A1 relevant to Figure 1 with information of chi-squared test. Panel (d) and (e) show the number of degrees of freedom (NDF) and the chi-square χ^2, respectively, versus relative energy $E_{^7\mathrm{Li}\text{-}p}$. The red dashed lines

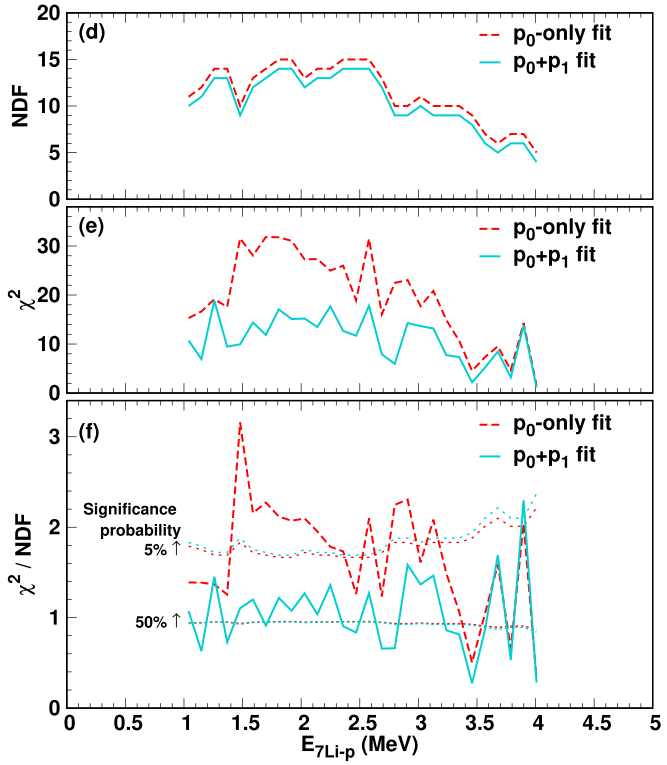

Figure A1. Chi-squared test for the p_0- and p_1-channel extraction.

represent the "p_0-only" fit, assuming that there is only p_0 contribution with a single Gaussian function peaked at the $Q_0^{3\text{-body}}$ (corresponding to "p_0" in Figure 1(b)), and the cyan solid lines represent the "$p_0 + p_1$" fit, employing a sum of two Gaussian functions peaked at $Q_0^{3\text{-body}}$ and $Q_1^{3\text{-body}}$ (corresponding to "$p_0 + p_1$" in Figure 1(b)). The reduced chi-square $\chi^2/$ NDF versus $E_{7\text{Li-}p}$ is then plotted in panel (f). Note that the only free parameters in the p_0-only and the $p_0 + p_1$ fits are the heights of the Gaussian functions, otherwise the peak positions and the widths are not fitted but fixed as functions of $E_{7\text{Li-}p}$, which are determined from the experimental data themselves of which $E_{7\text{Li-}p}$ dependency was confirmed by the simulation. That means that the difference between their NDFs is always 1 as seen in panel (d). One can see that the p_0-only χ^2 always tends to be larger than $p_0 + p_1$ below 3.5 MeV. The dotted lines in panel (f) indicate the upper significance probabilities of 50% and 5% for the NDFs as functions of $E_{7\text{Li-}p}$ for the p_0-only and $p_0 + p_1$ fits. This figure tells us that, if the p_0-only assumption is valid, such a χ^2 would appear only at a probability of less than 5% at most of the energies, which is obviously unlikely. On the other hand, the $p_0 + p_1$ fit χ^2 mostly settles around the 50% line, which means a "good" model. In conclusion, there is no reason to deny the existence of p_1 events, which can be evaluated quantitatively in a statistically reasonable way.

Appendix B
Adopted Cross Section Data Used for *R*-matrix Fit

The cross section data sets of the ^{7}Be(n, p_0)^{7}Li, ^{7}Be(n, p_1)^{7}Li*, and ^{7}Be(n, α)^{4}He reaction channels used for the *R*-matrix analysis are listed below with the selected center-of-mass energy ranges:

Table B1
Present Cross Section Data for the ^{7}Be(n, p_0)^{7}Li Reaction Channel

$E_{\text{c.m.}}$ (MeV)	σ (mb)	σ Error (mb)
1.7100E−01	3.2811E+03	7.2395E+02
2.2100E−01	3.2069E+03	6.7440E+02
2.7100E−01	3.2683E+03	6.5078E+02
3.2100E−01	4.6566E+03	8.4118E+02
3.7100E−01	2.9348E+03	5.5204E+02
4.2100E−01	2.0413E+03	4.2481E+02
4.7100E−01	1.4278E+03	3.2382E+02
5.2100E−01	1.1368E+03	2.6914E+02
5.7100E−01	9.5194E+02	2.4849E+02
6.2100E−01	9.6064E+02	2.3840E+02

Table B2
Present Cross Section Data for the ^{7}Be(n, p_1)^{7}Li* Reaction Channel

$E_{\text{c.m.}}$ (MeV)	σ (mb)	σ Error (mb)
5.0000E−02	1.0051E+03	4.3335E+02
1.5000E−01	7.9321E+02	3.0778E+02
2.5000E−01	2.7660E+02	1.7228E+02
3.5000E−01	4.9286E+02	1.8788E+02
4.5000E−01	8.7029E+02	2.0718E+02
5.5000E−01	7.6830E+02	1.7937E+02
6.5000E−01	4.0124E+02	1.3012E+02
7.5000E−01	5.1972E+02	1.4332E+02
8.5000E−01	3.5284E+02	1.1173E+02
9.5000E−01	1.9607E+02	7.3929E+01
1.0500E+00	2.6023E+02	7.7816E+01
1.1500E+00	1.6192E+02	5.8325E+01
1.2500E+00	2.0574E+02	6.6264E+01
1.3500E+00	1.1979E+02	5.3054E+01
1.4500E+00	2.3857E+02	6.4166E+01
1.5500E+00	1.1074E+02	4.5971E+01
1.6500E+00	1.7302E+02	5.4818E+01
1.7500E+00	1.2916E+02	5.0571E+01
1.8500E+00	1.2031E+02	5.1566E+01
1.9500E+00	9.9726E+01	4.2692E+01
2.0500E+00	1.0598E+02	4.6713E+01
2.1500E+00	7.9459E+01	3.6836E+01
2.2500E+00	5.8217E+01	3.2418E+01
2.3500E+00	4.0515E+01	4.3453E+01
2.4500E+00	5.5771E+01	3.8033E+01

1. (n, p_0): Dam18 (Damone et al. 2018, 1.79×10^{-8}–2.84×10^{-2} MeV), Sek76 (Sekharan et al. 1976, 3.09×10^{-2}–2.03 MeV), Bor63 (Borchers & Poppe 1963, 1.89–7.12 MeV), Pop76 (Poppe et al. 1976, 1.98–20.9 MeV), Present (Table B1, 1.71×10^{-1}–6.21×10^{-1} MeV).
2. (n, p_1): Koe88 renormalized by Dam18 (Koehler et al. 1988; Damone et al. 2018, 2.41×10^{-8}–5.36×10^{-5} MeV), Present (Table B2, 5.00×10^{-2}–1.75 MeV).
3. (n, α): Hou15 (Hou et al. 2015, 1.13×10^{-2}–5.75 MeV), Kaw17 (Kawabata et al. 2017, 2.21×10^{-1}–7.48×10^{-1} MeV), Lam17d (Lamia et al. 2017, 8.44×10^{-2}–4.07 MeV), Lam17^{3}He (Lamia et al. 2017, 1.03×10^{-1}–5.29 MeV), Lam19 (Lamia et al. 2019, 2.70×10^{-2}–1.71 MeV), Present (Table B3, 4.55×10^{-2}–1.95 MeV).

These present data are tabulated in Tables B1, B2, and B3, respectively.

Table B3
Present Cross Section Data for the ^{7}Be(n, α)^{4}He Reaction Channel

$E_{\rm c.m.}$ (MeV)	σ (mb)	σ Error (mb)
4.5455E−02	1.8920E+01	8.0471E+00
1.3636E−01	2.3730E+01	1.0252E+01
2.2727E−01	1.7352E+01	7.8241E+00
3.1818E−01	4.8899E+01	2.0648E+01
4.0909E−01	3.4661E+01	1.4974E+01
5.0000E−01	5.7867E+01	2.4435E+01
5.9091E−01	6.1183E+01	2.5835E+01
6.8182E−01	5.4730E+01	2.3276E+01
7.7273E−01	6.5180E+01	2.7523E+01
8.6364E−01	7.8637E+01	3.3022E+01
9.5455E−01	9.5229E+01	3.9814E+01
1.0455E+00	4.5928E+01	1.9989E+01
1.1364E+00	7.0944E+01	3.0172E+01
1.2273E+00	7.4196E+01	3.1555E+01
1.3182E+00	6.1473E+01	2.6558E+01
1.4091E+00	9.8541E+01	4.1611E+01
1.5000E+00	8.5586E+01	3.6560E+01
1.5909E+00	5.9830E+01	2.6277E+01
1.6818E+00	7.6157E+01	3.3146E+01
1.7727E+00	4.7037E+01	2.1640E+01
1.8636E+00	2.0911E+01	1.1196E+01
1.9546E+00	2.2840E+01	1.2229E+01

Appendix C
Details on the *R*-matrix Fit

We here give a supplemental description of the *R*-matrix fit. The levels above IV are labeled as V–X in serial order. This attempt of *R*-matrix analysis in a wide energy range ($E_{\rm c.m.} < 5$ MeV) rather emphasizes that the cross sections in the BBN-relevant energy region ($E_{\rm c.m.} < 0.6$ MeV) are characterized almost only by the first few resonances up to level IV, but is not to discuss the uniqueness of the fit at higher energies where the levels overlap each other more substantially. Figure C1 illustrates the level scheme of ^{8}Be excitation energy above the ^{7}Be + n threshold. Table C1 shows all the resonance parameters resulted from the *R*-matrix fit. Detailed explanations for each excited levels of ^{8}Be excitation used for the *R*-matrix analysis are given below.

1. Level I (2^{-}, $E_x = 18.91$ MeV): This is considered as the most responsible resonance for the enhancement of the (n, p_0) cross section above the neutron threshold up to the BBN-relevant energies. The parameterization conforms to that of Adahchour & Descouvemont (2003), namely, $\Gamma = \Gamma_n + \Gamma_p = \Gamma_n + \Gamma_{p0} + \Gamma_{p1}$, although the Γ_{p1} was found to be negligible from the fit. The Γ_α is not allowed by the parity conservation law for this excited state. Another *R*-matrix analysis by Koehler et al. (1988) defines the resonance energy and width as the properties of a pole of the *S*-matrix in the so-called Riemann sheet IV, which provides much smaller total width as adopted in Tilley et al. (2004). The energy and partial widths could not be determined simultaneously from the behavior of the (n, p_0) excitation function near the neutron threshold. We fixed the resonance energy at $E_x = 19.10$ MeV (Tilley et al. 2004) and free the widths, rather than fixing the widths and freeing the energy as Adahchour & Descouvemont (2003) did because the cross section varies sensitively to the resonance energy, which is so close to the threshold. Note that Adahchour & Descouvemont (2003) and Koehler et al. (1988) analyses were based on Koe88 p_0 data (Koehler et al. 1988) in the level-I dominant energy region, while we performed the fit to Dam18 p_0 data (Damone et al. 2018), which resulted in different fitted parameters. As long as the existence of level I is only assumed in this energy region, the fitted excitation function was always found to settle lower than the single-level Breit–Wigner resonance fit (p_0 Dam18 SLBW fit) by Damone et al. (2018) especially around $E_{\rm c.m.} = 10$ keV no matter if all the level I parameters are freed or some are fixed. This is nothing but because p_0 Dam18 SLBW fit allows anomalistically large Γ_n of level

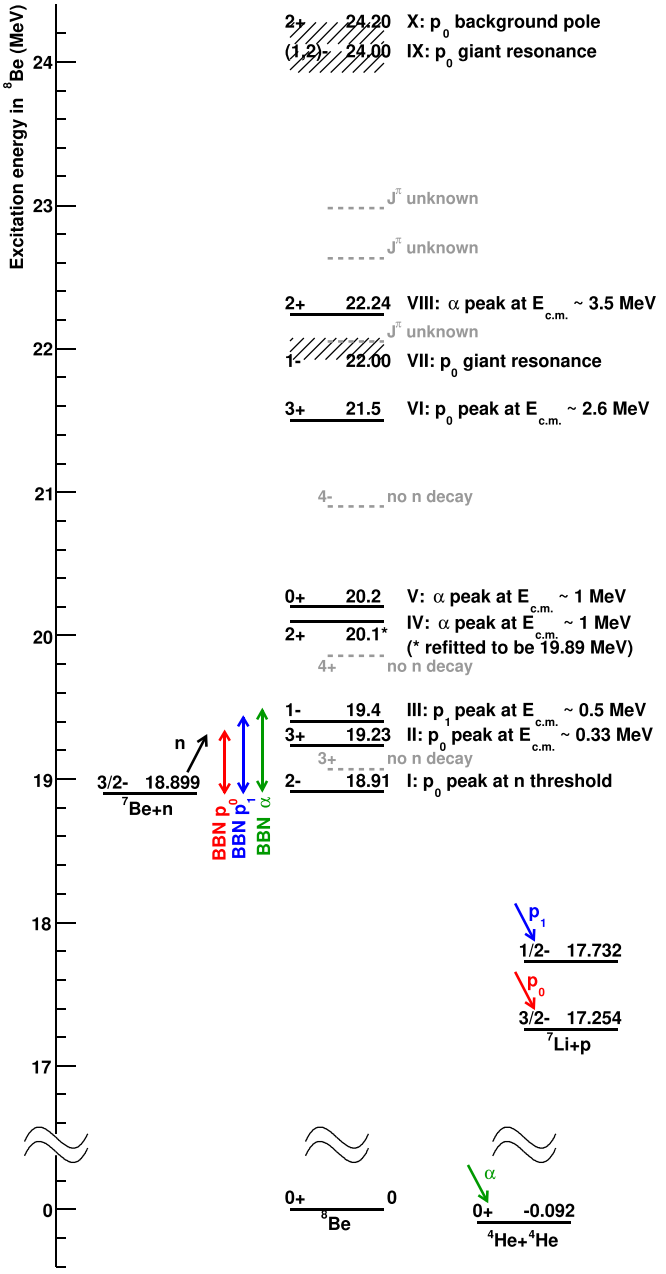

Figure C1. Level scheme of the ^{8}Be excitation energy above the ^{7}Be + n threshold. The levels adopted in the *R*-matrix analysis are shown as black solid lines, and the ones not adopted are shown as gray dashed lines. The adopted broad levels are shown in black hatch. The effective energy ranges to the BBN for each decay channel are indicated by colored vertical arrows. The typical contributions are briefly explained on the right-hand side of each level.

Table C1
Resonance Parameters of All the ^{8}Be Excited Levels Used in the *R*-matrix Fit

Level No.	J^{π}	E_x	$E_{\rm c.m.}$	l_n	Γ_n	l_{p0}	Γ_{p0}	l_{p1}	Γ_{p1}	l_α	Γ_α	Γ	$\Gamma^{\rm (Ref.)}$
I	2^-	18910[a]	10	0	297^{+23}_{-32}	0	651^{+55}_{-73}	2	$\sim$0	⋯	⋯	948^{+59}_{-80}	1634[b]
II	3^+	19230[b]	330	1	89^{+8}_{-9}	1	66^{+4}_{-3}	3	$\sim$0	⋯	⋯	155^{+9}_{-10}	165[b]
III	1^-	19400[a]	500	0	263^{+56}_{-46}	0	$\sim$0	0	326^{+75}_{-70}	⋯	⋯	589^{+94}_{-84}	645[a]
IV	2^+	$(19885^{\pm 20})$	$(985^{\pm 20})$	1	$(89^{\pm 3})$	1	23[c]	1	143[c]	2	726[c]	(981)	880[a]
V	0^+	20200[a]	1300	1	260[d]	1	50[d]	1	50[d]	0	360[d]	720[d]	720[a]
VI	3^+	21500[b]	2600	1	490[b]	1	610[b]	3	0[d]	⋯	⋯	1100[d]	1100[b]
VII	1^-	22000[a]	3100	0	(300^{+92}_{-79})	0	(303^{+96}_{-83})	0	($\sim$0)	⋯	⋯	(602^{+132}_{-115})	$\sim$4000[a]
VIII	2^+	22240[a]	3340	1	(351^{+16}_{-15})	1	($\sim$0)	1	($\sim$0)	2	$(559^{\pm 32})$	$(910^{\pm 36})$	$\sim$800[a]
IX	2^-	24000[a]	5100	0	(10020^{+860}_{-820})	0	(2830^{+500}_{-370})	2	($\sim$0)	⋯	⋯	(12850^{+1000}_{-900})	$\sim$7000[a]
X	2^+	24200[d]	5300	1	(43200^{+3400}_{-3000})	1	(37000^{+3300}_{-2900})	1	0[d]	2	0[d]	(80200^{+4700}_{-4200})	

Notes. The brackets indicate provisional fit values. Energies are all in units of keV.
[a] From Tilley et al. (2004).
[b] From Adahchour & Descouvemont (2003).
[c] The proton and α widths of Level IV are fixed at a ratio $\Gamma_\alpha/\Gamma_p \sim 4.5$ (Tilley et al. 2004).
[d] Fixed at an arbitrary value during the fitting process.

III (about 2.6 times larger than the Wigner limit) to contribute to the cross section in this energy region. We stress that the uncertainty of the fitted (n, p_0) cross section appears to well reproduce those of Dam18 p_0 data points.

2. Level II (3^+, $E_x = 19.23$ MeV): We fix the resonance energy at $E_{\rm c.m.} = 330$ keV as done in Adahchour & Descouvemont (2003), and obtain similar partial widths Γ_n and Γ_{p0} to their values.
3. Level III (1^-, $E_x = 19.4$ MeV): This *s*-wave state should be the only significant resonance to describe both the present and Koe88 p_1 data (renormalized to Dam18), which peak around $E_{\rm c.m.} = 500$ keV and tail down to the thermal neutron energy by the $1/v$ law. From this fit, the Γ_n and Γ_{p1} are comparable to maximize the resonance, which does not leave room for Γ_{p0} to be significant. The higher-energy tail of the (n, p_1) resonance around $E_{\rm c.m.} = 500$ keV implies necessity of some contributions from higher-lying levels for a better fit and/or a more accurate measurement.
4. Level IV (2^+, $E_x = 20.1$ MeV, refitted to be 19.885 ± 0.02 MeV): This *p*-wave level is considered responsible for the first significant resonance in the (n, α) channel above the neutron threshold, forming the peak around $E_{\rm c.m.} = 1$ MeV. However, the contribution of this resonance to the (n, p_0) and (n, p_1) cross sections is not as significant. The neighbor level (4^+ at $E_x = 19.86$ MeV) does not contribute as much due to its high spin nature. The (n, α) data have somewhat large variations to be fitted uniquely together with the (n, p_0) and the (n, p_1) channels at the same time. Therefore, we fixed the Γ_{p0}, Γ_{p1}, and Γ_α at the known ratio $\Gamma_p/\Gamma_\alpha \sim 4.5 \pm 0.6$ (Tilley et al. 2004), and freed Γ_n. The resonance energy is also freed to better reproduce the lower energy tail of the resonance, otherwise the total width Γ tends to much larger than the known value of 880 keV. Such a treatment may provide only a provisional result, but simplifies the analysis to focus on the more dominant channels (n, p_0) and (n, p_1).
5. Level V (0^+, $E_x = 20.2$ MeV): This level may provide an additional contribution to better reproduce the higher-energy tail of the $E_{\rm c.m.} = 1$ MeV peak in the (n, α) channel, although it is not significant in the (n, p_0) and the (n, p_1) channels either. We fix all the partial widths due to the same motivation as level IV, with constraints of $\Gamma = 720$ MeV and $\Gamma_\alpha/\Gamma < 0.5$ (Tilley et al. 2004).
6. Level VI (3^+, $E_x = 21.5$ MeV): This level forms the resonances in the (n, p_0) channel around $E_{\rm c.m.} = 2.6$ MeV. We adopted the same energy and widths from Adahchour & Descouvemont (2003).
7. Level VII (1^-, $E_x = 22.0$ MeV): This is known as a giant resonance (Tilley et al. 2004). Although no neutron emission decay is known from this state, we included it by the necessity of *s*-wave resonances to reproduce the enhancement of the (n, p_0) cross sections above $E_{\rm c.m.} \sim 0.6$ MeV. The obtained total width Γ is, however, much smaller than the known value ($\approx$4 MeV; Tilley et al. 2004). Since the broad levels in this energy region overlap each other significantly, this could be a consequence of large Γ of the higher-lying levels such as IX and X.
8. Level VIII (2^+, $E_x = 22.24$ MeV): This level is responsible for the second resonance in the (n, α) channel around $E_{\rm c.m.} = 3.5$ MeV. The gap between the first and the second resonances in the (n, α) channel may be formed by the interference between this state and level IV. Although the fitted total Γ is eventually consistent with the known value of 800 keV (Tilley et al. 2004), the higher-energy tail of the (n, α) second resonance looks still wider, which might suggest the participation of some more excited levels.
9. Level IX ($(1, 2)^-$, 2^- assumed, $E_x = 24.0$ MeV): The spin and parity of this giant resonance is assigned as $(1, 2)^-$ (Tilley et al. 2004), and no neutron emission decay is known. We include this level assuming the spin and parity of 2^- by the same motivation as level VII. A significantly larger Γ than the known value ($\approx$7 MeV) emerges, which might be the reason to reduce the Γ of lower-lying level VII instead.
10. Level X (2^+, $E_x = 24.2$ MeV): As well as the treatment done by Adahchour & Descouvemont (2003), a 2^+ background pole is induced at an arbitrarily high energy ($E_x = 24.2$ MeV in the present analysis), and Γ_n and Γ_{p0} are fitted.

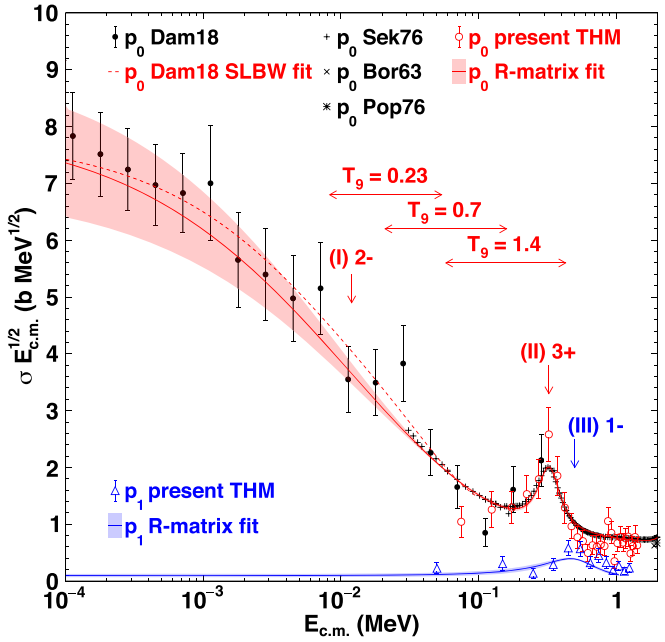

Figure D1. Enlarged view of Figure 2 with the vertical axis in linear scale for a better comparison of p_0 Dam18 SLBW fit (red dashed line) and the present p_0 R-matrix fit (red solid line). The horizontal arrows are intended to specify important energy ranges corresponding to the BBN temperature ranges of $T_9 = 0.23$–1.4.

Appendix D
Detailed Comparison of the ^{7}Be$(n, p_0)^7$Li Cross Sections

An enlarged figure for the (n, p_0) cross sections in an energy range of $E_{\rm c.m.} = 1 \times 10^{-4}$–2 MeV is shown in Figure D1 together with the (n, p_1) cross sections for comparison. The vertical axis is in linear scale to better compare the p_0 Dam18 SLBW fit (red dashed line; Damone et al. 2018) and the present p_0 R-matrix fit (red solid line). The horizontal arrows are intended to specify important energy ranges corresponding to the BBN temperature ranges of $T_9 = 0.23$–1.4.

Appendix E
Recommended ^{7}Be$(n, p)^7$Li Reaction Rate

The sum of the present (n, p_0) and (n, p_1) reaction rates as a function of temperature T_9 can be expressed by the same analytic formula as in Damone et al. (2018) and Smith et al. (1993) with a power expansion in T_9 (coefficients a_0 to a_5), an exponential term (a_6), and a resonance term (a_7):

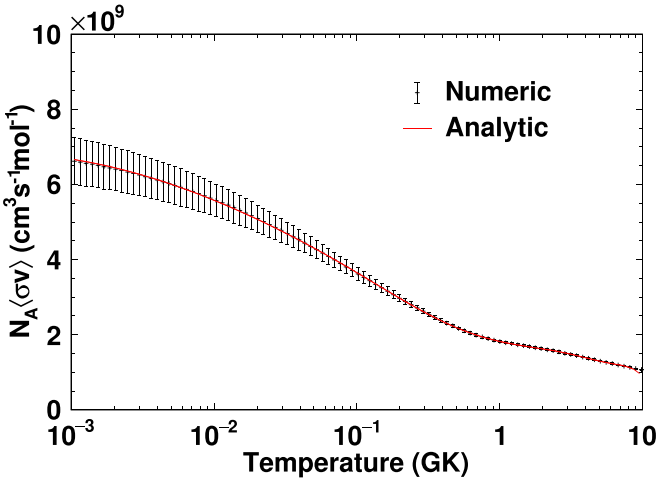

Figure E1. The present $(n, p_0) + (n, p_1)$ reaction rates of the original numerical calculation from the R-matrix result (black dots), and the fitted analytic formula (Equation E1; red solid curve).

$$N_{\rm A}\langle v\sigma\rangle = a_0(1 + a_1 T_9^{1/2} + a_2 T_9 + a_3 T_9^{3/2} + a_4 T_9^2 + a_5 T_9^{5/2}) + a_6\left(\frac{1}{1 + T_9/b_0}\right)^{3/2} + a_7 T_9^{-3/2} e^{-b_1/T_9}, \quad \text{(E1)}$$

in units of cm^3 s^{-1} mole^{-1}, where the fitted coefficients are

$$\begin{aligned} a_0 &= 6.52764 \times 10^9, \\ a_1 &= -1.96386, \\ a_2 &= 2.11477, \\ a_3 &= -1.14397, \\ a_4 &= 3.00976 \times 10^{-1}, \\ a_5 &= -3.07557 \times 10^{-2}, \\ a_6 &= 6.36429 \times 10^8, \\ a_7 &= 1.09224 \times 10^8, \\ b_0 &= 8.63439 \times 10^{-3}, \\ b_1 &= 2.31642. \end{aligned}$$

The fit guarantees good precision ($<\pm 0.5\%$ deviation) at least above $T_9 = 10^{-3}$ up to $T_9 = 8$. The fitted function to the

Table E1
Present ^{7}Be(n, p_0)^{7}Li Reaction Rate

T_9	$N_A\langle\sigma v\rangle$ ($cm^3\ s^{-1}\ mole^{-1}$)	$N_A\langle\sigma v\rangle$ Error ($cm^3\ s^{-1}\ mole^{-1}$)
1.0510e−03	6.5502e+09	8.2725e+08
1.1560e−03	6.5219e+09	8.2462e+08
1.2720e−03	6.4922e+09	8.1528e+08
1.3990e−03	6.4624e+09	8.1133e+08
1.5390e−03	6.4304e+09	7.9981e+08
1.6930e−03	6.3974e+09	7.9554e+08
1.8620e−03	6.3658e+09	7.8465e+08
2.0480e−03	6.3270e+09	7.7650e+08
2.2530e−03	6.2924e+09	7.6625e+08
2.4790e−03	6.2553e+09	7.5732e+08
2.7260e−03	6.2166e+09	7.4334e+08
2.9990e−03	6.1738e+09	7.3586e+08
3.2990e−03	6.1328e+09	7.2444e+08
3.6290e−03	6.0859e+09	7.1633e+08
3.9920e−03	6.0414e+09	7.0407e+08
4.3910e−03	5.9946e+09	6.9394e+08
4.8300e−03	5.9480e+09	6.7995e+08
5.3130e−03	5.8949e+09	6.6962e+08
5.8440e−03	5.8427e+09	6.5755e+08
6.4290e−03	5.7902e+09	6.4331e+08
7.0720e−03	5.7334e+09	6.3220e+08
7.7790e−03	5.6765e+09	6.1699e+08
8.5570e−03	5.6159e+09	6.0517e+08
9.4120e−03	5.5553e+09	5.9250e+08
1.0350e−02	5.4928e+09	5.7978e+08
1.1390e−02	5.4270e+09	5.6176e+08
1.2530e−02	5.3609e+09	5.5033e+08
1.3780e−02	5.2935e+09	5.3391e+08
1.5160e−02	5.2256e+09	5.2135e+08
1.6670e−02	5.1546e+09	5.0706e+08
1.8340e−02	5.0799e+09	4.9016e+08
2.0180e−02	5.0030e+09	4.7319e+08
2.2190e−02	4.9283e+09	4.5734e+08
2.4410e−02	4.8479e+09	4.4185e+08
2.6850e−02	4.7687e+09	4.2629e+08
2.9540e−02	4.6884e+09	4.1317e+08
3.2490e−02	4.6044e+09	3.9330e+08
3.5740e−02	4.5209e+09	3.7745e+08
3.9320e−02	4.4356e+09	3.6205e+08
4.3250e−02	4.3475e+09	3.4560e+08
4.7570e−02	4.2610e+09	3.3098e+08
5.2330e−02	4.1712e+09	3.1484e+08
5.7570e−02	4.0814e+09	3.0131e+08
6.3320e−02	3.9897e+09	2.8271e+08
6.9650e−02	3.8984e+09	2.6792e+08
7.6620e−02	3.8055e+09	2.5375e+08
8.4280e−02	3.7124e+09	2.3800e+08
9.2710e−02	3.6193e+09	2.2327e+08
1.0200e−01	3.5254e+09	2.0904e+08
1.1220e−01	3.4319e+09	1.9553e+08
1.2340e−01	3.3376e+09	1.8129e+08
1.3570e−01	3.2445e+09	1.6910e+08
1.4930e−01	3.1509e+09	1.5532e+08
1.6420e−01	3.0583e+09	1.4341e+08
1.8070e−01	2.9657e+09	1.3142e+08
1.9870e−01	2.8743e+09	1.1968e+08
2.1860e−01	2.7837e+09	1.0932e+08
2.4050e−01	2.6942e+09	9.7824e+07
2.6450e−01	2.6066e+09	8.8737e+07
2.9100e−01	2.5203e+09	8.1484e+07
3.2010e−01	2.4362e+09	7.3641e+07
3.5210e−01	2.3513e+09	6.2026e+07
3.8730e−01	2.2702e+09	5.3556e+07

Table E1
(Continued)

T_9	$N_A\langle\sigma v\rangle$ ($cm^3\ s^{-1}\ mole^{-1}$)	$N_A\langle\sigma v\rangle$ Error ($cm^3\ s^{-1}\ mole^{-1}$)
4.2600e−01	2.1918e+09	4.4911e+07
4.6860e−01	2.1193e+09	4.3252e+07
5.1550e−01	2.0439e+09	3.3433e+07
5.6700e−01	1.9783e+09	2.8153e+07
6.2370e−01	1.9145e+09	2.1998e+07
6.8610e−01	1.8564e+09	1.4883e+07
7.5470e−01	1.8025e+09	1.1881e+07
8.3010e−01	1.7509e+09	1.0517e+07
9.1320e−01	1.7035e+09	9.8630e+06
1.0040e+00	1.6603e+09	9.5275e+06
1.1050e+00	1.6206e+09	9.4185e+06
1.2150e+00	1.5835e+09	9.8980e+06
1.3370e+00	1.5485e+09	1.0537e+07
1.4710e+00	1.5146e+09	1.1389e+07
1.6180e+00	1.4814e+09	1.2629e+07
1.7790e+00	1.4482e+09	1.3622e+07
1.9570e+00	1.4145e+09	1.4778e+07
2.1530e+00	1.3804e+09	1.5752e+07
2.3690e+00	1.3455e+09	1.6366e+07
2.6050e+00	1.3100e+09	1.7093e+07
2.8660e+00	1.2740e+09	1.7361e+07
3.1520e+00	1.2375e+09	1.7301e+07
3.4680e+00	1.2012e+09	1.7333e+07
3.8150e+00	1.1652e+09	1.7572e+07
4.1960e+00	1.1301e+09	1.6949e+07
4.6160e+00	1.0960e+09	1.6267e+07
5.0770e+00	1.0634e+09	1.5768e+07
5.5850e+00	1.0323e+09	1.5039e+07
6.1430e+00	1.0029e+09	1.4321e+07
6.7580e+00	9.7590e+08	1.3273e+07
7.4330e+00	9.5035e+08	1.2406e+07
8.1770e+00	9.2623e+08	1.1581e+07
8.9940e+00	9.0328e+08	1.0746e+07
9.8940e+00	8.7997e+08	1.1770e+07

Table E2
Present ^{7}Be(n, p_1)^{7}Li* Reaction Rate

T_9	$N_A\langle\sigma v\rangle$ ($cm^3\ s^{-1}\ mole^{-1}$)	$N_A\langle\sigma v\rangle$ Error ($cm^3\ s^{-1}\ mole^{-1}$)
1.0510e−03	8.7351e+07	2.3590e+07
1.1560e−03	8.7349e+07	2.3588e+07
1.2720e−03	8.7348e+07	2.3586e+07
1.3990e−03	8.7347e+07	2.3586e+07
1.5390e−03	8.7296e+07	2.3497e+07
1.6930e−03	8.7445e+07	2.3716e+07
1.8620e−03	8.7456e+07	2.3857e+07
2.0480e−03	8.7404e+07	2.3591e+07
2.2530e−03	8.7453e+07	2.3850e+07
2.4790e−03	8.7395e+07	2.3562e+07
2.7260e−03	8.7453e+07	2.3846e+07
2.9990e−03	8.7394e+07	2.3561e+07
3.2990e−03	8.7447e+07	2.3821e+07
3.6290e−03	8.7364e+07	2.3513e+07
3.9920e−03	8.7447e+07	2.3694e+07
4.3910e−03	8.7454e+07	2.3812e+07
4.8300e−03	8.7356e+07	2.3473e+07
5.3130e−03	8.7430e+07	2.3608e+07
5.8440e−03	8.7471e+07	2.3796e+07
6.4290e−03	8.7381e+07	2.3454e+07

Table E2
(Continued)

T_9	$N_A\langle\sigma v\rangle$ ($cm^3\ s^{-1}\ mole^{-1}$)	$N_A\langle\sigma v\rangle$ Error ($cm^3\ s^{-1}\ mole^{-1}$)
7.0720e−03	8.7449e+07	2.3585e+07
7.7790e−03	8.7544e+07	2.3847e+07
8.5570e−03	8.7415e+07	2.3446e+07
9.4120e−03	8.7485e+07	2.3564e+07
1.0350e−02	8.7587e+07	2.3839e+07
1.1390e−02	8.7464e+07	2.3439e+07
1.2530e−02	8.7567e+07	2.3548e+07
1.3780e−02	8.7598e+07	2.3547e+07
1.5160e−02	8.7625e+07	2.3539e+07
1.6670e−02	8.7668e+07	2.3535e+07
1.8340e−02	8.7726e+07	2.3548e+07
2.0180e−02	8.7784e+07	2.3538e+07
2.2190e−02	8.7830e+07	2.3537e+07
2.4410e−02	8.7889e+07	2.3542e+07
2.6850e−02	8.7967e+07	2.3549e+07
2.9540e−02	8.8056e+07	2.3551e+07
3.2490e−02	8.8142e+07	2.3558e+07
3.5740e−02	8.8193e+07	2.3523e+07
3.9320e−02	8.8267e+07	2.3457e+07
4.3250e−02	8.8408e+07	2.3461e+07
4.7570e−02	8.8781e+07	2.3873e+07
5.2330e−02	8.8835e+07	2.3689e+07
5.7570e−02	8.9036e+07	2.3577e+07
6.3320e−02	8.9192e+07	2.3576e+07
6.9650e−02	8.9355e+07	2.3477e+07
7.6620e−02	8.9909e+07	2.3941e+07
8.4280e−02	9.0111e+07	2.3802e+07
9.2710e−02	9.0376e+07	2.3697e+07
1.0200e−01	9.0862e+07	2.4043e+07
1.1220e−01	9.1226e+07	2.3878e+07
1.2340e−01	9.1822e+07	2.4201e+07
1.3570e−01	9.2268e+07	2.3984e+07
1.4930e−01	9.2963e+07	2.4219e+07
1.6420e−01	9.3569e+07	2.4181e+07
1.8070e−01	9.4403e+07	2.4365e+07
1.9870e−01	9.5299e+07	2.4714e+07
2.1860e−01	9.6156e+07	2.4568e+07
2.4050e−01	9.7333e+07	2.4968e+07
2.6450e−01	9.8517e+07	2.4856e+07
2.9100e−01	1.0001e+08	2.5351e+07
3.2010e−01	1.0149e+08	2.5179e+07
3.5210e−01	1.0332e+08	2.5488e+07
3.8730e−01	1.0541e+08	2.5713e+07
4.2600e−01	1.0766e+08	2.5916e+07
4.6860e−01	1.1034e+08	2.6261e+07
5.1550e−01	1.1343e+08	2.6610e+07
5.6700e−01	1.1686e+08	2.6720e+07
6.2370e−01	1.2083e+08	2.7118e+07
6.8610e−01	1.2528e+08	2.7352e+07
7.5470e−01	1.3012e+08	2.7210e+07
8.3010e−01	1.3581e+08	2.7775e+07
9.1320e−01	1.4178e+08	2.7395e+07
1.0040e+00	1.4851e+08	2.7515e+07
1.1050e+00	1.5552e+08	2.7327e+07
1.2150e+00	1.6330e+08	2.7641e+07
1.3370e+00	1.7078e+08	2.6520e+07
1.4710e+00	1.7876e+08	2.6122e+07
1.6180e+00	1.8690e+08	2.5889e+07
1.7790e+00	1.9453e+08	2.4974e+07
1.9570e+00	2.0203e+08	2.4220e+07
2.1530e+00	2.0896e+08	2.3392e+07
2.3690e+00	2.1515e+08	2.2309e+07
2.6050e+00	2.2052e+08	2.1355e+07
2.8660e+00	2.2500e+08	2.0238e+07

Table E2
(Continued)

T_9	$N_A\langle\sigma v\rangle$ ($cm^3\ s^{-1}\ mole^{-1}$)	$N_A\langle\sigma v\rangle$ Error ($cm^3\ s^{-1}\ mole^{-1}$)
3.1520e+00	2.2839e+08	1.9038e+07
3.4680e+00	2.3075e+08	1.8114e+07
3.8150e+00	2.3196e+08	1.6844e+07
4.1960e+00	2.3191e+08	1.5708e+07
4.6160e+00	2.3074e+08	1.4558e+07
5.0770e+00	2.2833e+08	1.3296e+07
5.5850e+00	2.2484e+08	1.2327e+07
6.1430e+00	2.2012e+08	1.1113e+07
6.7580e+00	2.1440e+08	1.0204e+07
7.4330e+00	2.0764e+08	9.3101e+06
8.1770e+00	1.9998e+08	8.3395e+06
8.9940e+00	1.9150e+08	7.5576e+06
9.8940e+00	1.8240e+08	6.7788e+06

Table E3
Present $^7Be(n, p_0)^7Li + {}^7Be(n, p_1)^7Li^*$ Reaction Rate

T_9	$N_A\langle\sigma v\rangle$ ($cm^3\ s^{-1}\ mole^{-1}$)	$N_A\langle\sigma v\rangle$ Error ($cm^3\ s^{-1}\ mole^{-1}$)
1.0510E−03	6.6376E+09	8.2759E+08
1.1560E−03	6.6092E+09	8.2496E+08
1.2720E−03	6.5795E+09	8.1562E+08
1.3990E−03	6.5497E+09	8.1167E+08
1.5390E−03	6.5177E+09	8.0016E+08
1.6930E−03	6.4848E+09	7.9589E+08
1.8620E−03	6.4533E+09	7.8501E+08
2.0480E−03	6.4144E+09	7.7686E+08
2.2530E−03	6.3799E+09	7.6662E+08
2.4790E−03	6.3427E+09	7.5769E+08
2.7260E−03	6.3041E+09	7.4372E+08
2.9990E−03	6.2612E+09	7.3624E+08
3.2990E−03	6.2202E+09	7.2483E+08
3.6290E−03	6.1733E+09	7.1672E+08
3.9920E−03	6.1288E+09	7.0447E+08
4.3910E−03	6.0821E+09	6.9435E+08
4.8300E−03	6.0354E+09	6.8036E+08
5.3130E−03	5.9823E+09	6.7004E+08
5.8440E−03	5.9302E+09	6.5798E+08
6.4290E−03	5.8776E+09	6.4374E+08
7.0720E−03	5.8208E+09	6.3264E+08
7.7790E−03	5.7640E+09	6.1745E+08
8.5570E−03	5.7033E+09	6.0562E+08
9.4120E−03	5.6428E+09	5.9297E+08
1.0350E−02	5.5804E+09	5.8027E+08
1.1390E−02	5.5145E+09	5.6225E+08
1.2530E−02	5.4485E+09	5.5083E+08
1.3780E−02	5.3811E+09	5.3443E+08
1.5160E−02	5.3132E+09	5.2188E+08
1.6670E−02	5.2423E+09	5.0761E+08
1.8340E−02	5.1676E+09	4.9073E+08
2.0180E−02	5.0908E+09	4.7378E+08
2.2190E−02	5.0161E+09	4.5795E+08
2.4410E−02	4.9358E+09	4.4248E+08
2.6850E−02	4.8567E+09	4.2694E+08
2.9540E−02	4.7765E+09	4.1384E+08
3.2490E−02	4.6925E+09	3.9400E+08
3.5740E−02	4.6091E+09	3.7818E+08
3.9320E−02	4.5239E+09	3.6281E+08
4.3250E−02	4.4359E+09	3.4640E+08
4.7570E−02	4.3498E+09	3.3184E+08
5.2330E−02	4.2600E+09	3.1573E+08

Table E3
(Continued)

T_9	$N_A\langle\sigma v\rangle$ ($cm^3\ s^{-1}\ mole^{-1}$)	$N_A\langle\sigma v\rangle$ Error ($cm^3\ s^{-1}\ mole^{-1}$)
5.7570E−02	4.1704E+09	3.0223E+08
6.3320E−02	4.0789E+09	2.8369E+08
6.9650E−02	3.9878E+09	2.6895E+08
7.6620E−02	3.8954E+09	2.5488E+08
8.4280E−02	3.8025E+09	2.3919E+08
9.2710E−02	3.7097E+09	2.2452E+08
1.0200E−01	3.6163E+09	2.1042E+08
1.1220E−01	3.5231E+09	1.9698E+08
1.2340E−01	3.4294E+09	1.8290E+08
1.3570E−01	3.3368E+09	1.7079E+08
1.4930E−01	3.2439E+09	1.5720E+08
1.6420E−01	3.1519E+09	1.4543E+08
1.8070E−01	3.0601E+09	1.3366E+08
1.9870E−01	2.9696E+09	1.2221E+08
2.1860E−01	2.8799E+09	1.1205E+08
2.4050E−01	2.7915E+09	1.0096E+08
2.6450E−01	2.7051E+09	9.2152E+07
2.9100E−01	2.6203E+09	8.5336E+07
3.2010E−01	2.5377E+09	7.7827E+07
3.5210E−01	2.4546E+09	6.7059E+07
3.8730E−01	2.3756E+09	5.9409E+07
4.2600E−01	2.2995E+09	5.1852E+07
4.6860E−01	2.2296E+09	5.0600E+07
5.1550E−01	2.1573E+09	4.2730E+07
5.6700E−01	2.0952E+09	3.8814E+07
6.2370E−01	2.0353E+09	3.4918E+07
6.8610E−01	1.9817E+09	3.1139E+07
7.5470E−01	1.9326E+09	2.9691E+07
8.3010E−01	1.8867E+09	2.9699E+07
9.1320E−01	1.8453E+09	2.9116E+07
1.0040E+00	1.8088E+09	2.9118E+07
1.1050E+00	1.7761E+09	2.8905E+07
1.2150E+00	1.7468E+09	2.9360E+07
1.3370E+00	1.7193E+09	2.8537E+07
1.4710E+00	1.6934E+09	2.8497E+07
1.6180E+00	1.6683E+09	2.8805E+07
1.7790E+00	1.6427E+09	2.8447E+07
1.9570E+00	1.6165E+09	2.8372E+07
2.1530E+00	1.5894E+09	2.8201E+07
2.3690E+00	1.5607E+09	2.7668E+07
2.6050E+00	1.5305E+09	2.7353E+07
2.8660E+00	1.4990E+09	2.6664E+07
3.1520E+00	1.4659E+09	2.5725E+07
3.4680E+00	1.4320E+09	2.5071E+07
3.8150E+00	1.3972E+09	2.4341E+07
4.1960E+00	1.3620E+09	2.3109E+07
4.6160E+00	1.3267E+09	2.1830E+07
5.0770E+00	1.2917E+09	2.0626E+07
5.5850E+00	1.2571E+09	1.9445E+07
6.1430E+00	1.2230E+09	1.8127E+07
6.7580E+00	1.1903E+09	1.6742E+07
7.4330E+00	1.1580E+09	1.5511E+07
8.1770E+00	1.1262E+09	1.4271E+07
8.9940E+00	1.0948E+09	1.3137E+07
9.8940E+00	1.0624E+09	1.3583E+07

present $(n, p_0) + (n, p_1)$ reaction rate of the original numeric calculation is shown in Figure E1.

The present reaction rates of the (n, p_0) and (n, p_1) channels, and their sum are tabulated in Tables E1, E2, and E3, respectively, in a temperature range of $T_9 = 0.001$–10.

Appendix F
Condition for the BBN Calculations

The primordial nucleosynthesis calculations were carried out using the PRIMAT (PRImordial MATter) code (Pitrou 2018; Pitrou et al. 2018). It is a Wolfram Mathematica code that computes the abundances of elements at the end of the Big Bang nucleosynthesis and their uncertainties. Indeed, an important feature is the possibility to fully account for reaction rate uncertainties using a Monte Carlo technique (Coc et al. 2014). For each temperature, the reaction rate is assumed to be distributed according to a log-normal distribution. The use of a Monte Carlo approach makes it possible to take into consideration correlation effects, and to retrieve statistically significant uncertainties (1 standard deviation).

In our calculation, we considered 1000 Monte Carlo iterations for each $\eta = 10^n$, with n varying from −10 to −9 in steps of 0.05. As recommended by the authors, the same sequence of seed numbers is used to reduce Monte Carlo noise when evaluating uncertainty in rates. Among the results of the calculation, in the case of our work it is of special interest the resulting computed abundances, which are given as a set of interpolating functions of $\eta \times 10^{10}$ for the ratio to H of the abundances of D, ^{3}He, and ^{7}Li. The only changes we introduced in the code with respect to the one discussed in Pitrou et al. (2018) are the rates of the ^{7}Be$(n, p)^7$Li and of the ^{7}Be$(n, \alpha)^4$He reactions (the latter having a very negligible effect on the ^{7}Li/H ratio) as listed in Table 2.

ORCID iDs

S. Hayakawa https://orcid.org/0000-0002-2054-8423
M. La Cognata https://orcid.org/0000-0002-1819-4814
L. Lamia https://orcid.org/0000-0002-4055-0811
H. Yamaguchi https://orcid.org/0000-0001-9931-2052
D. Kahl https://orcid.org/0000-0003-3368-7307
N. Iwasa https://orcid.org/0000-0002-6023-5608
S. Kubono https://orcid.org/0000-0003-0783-5978
S. Palmerini https://orcid.org/0000-0001-5386-8389
R. G. Pizzone https://orcid.org/0000-0003-2436-6640

References

Adahchour, A., & Descouvemont, P. 2003, JPhG, 29, 395
Ade, P. A. R., Aghanim, N., Arnaud, M., et al. 2016, A&A, 594, A13
Arbey, A. 2012, CoPhC, 183, 1822
Azuma, R. E., Uberseder, E., Simpson, E. C., et al. 2010, PhRvC, 81, 045805
Barbagallo, M., Andrzejewski, J., Mastromarco, M., et al. 2018, NIMPA, 887, 27
Barbagallo, M., Musumarra, A., Cosentino, L., et al. 2016, PhRvL, 117, 152701
Baur, G. 1986, PhLB, 178, 135
Borchers, R. R., & Poppe, C. H. 1963, PhRv, 129, 2679
Cherubini, S., Gulino, M., Spitaleri, C., et al. 2015, PhRvC, 92, 015805
Coc, A., Uzan, J.-P., & Vangioni, E. 2014, JCAP, 10, 050
Coc, A., & Vangioni, E. 2017, IJMPE, 26, 1741002
Costanzo, E., Lattuada, M., Romano, S., Vinciguerra, D., & Zadro, M. 1990, NIMPA, 295, 373
Cyburt, R. H. 2004, PhRvD, 70, 023505
Cyburt, R. H., Fields, B. D., Olive, K. A., & Yeh, T. H. 2016, RvMP, 88, 015004
Damone, L., Barbagallo, M., Mastromarco, M., et al. 2018, PhRvL, 121, 042701
Damone, L. A. 2018, Supplemental Material for the ^{7}Be$(n,p)^7$Li Paper, https://twiki.cern.ch/twiki/bin/view/NTOFPublic/Be7npPaperDraft
de Souza, R. S., Kiat, T. H., Coc, A., & Iliadis, C. 2020, ApJ, 894, 134
Descouvemont, P., Adahchour, A., Angulo, C., Coc, A., & Vangioni-Flam, E. 2004, ADNDT, 88, 203
Farinon, F., Glodariu, T., Mazzocco, M., et al. 2008, NIMPB, 266, 4097

Fields, B. D. 2011, ARNPS, 61, 47
Gulino, M., Spitaleri, C., Cherubini, S., et al. 2010, JPhG, 37, 125105
Gulino, M., Spitaleri, C., Tang, X. D., et al. 2013, PhRvC, 87, 012801
Hou, S. Q., He, J. J., Kubono, S., & Chen, Y. S. 2015, PhRvC, 91, 055802
Kawabata, T., Fujikawa, Y., Furuno, T., et al. 2017, PhRvL, 118, 052701
Koehler, P., Bowman, C., Steinkruger, F., et al. 1988, PhRvC, 37, 917
Kubono, S., Yanagisawa, Y., Teranishi, T., et al. 2002, EPJA, 13, 217
Kumagai, H., Ozawa, A., Fukuda, N., et al. 2001, NIMPA, 470, 562
Lamia, L., Mazzocco, M., Pizzone, R. G., et al. 2019, ApJ, 879, 23
Lamia, L., Spitaleri, C., Bertulani, C. A., et al. 2017, ApJ, 850, 175
Pitrou, C. 2018, PRIMAT—PRImordial MATter, http://www2.iap.fr/users/pitrou/primat.htm
Pitrou, C., Coc, A., Uzan, J. P., & Vangioni, E. 2018, PhR, 754, 1
Pizzone, R. G., Roeder, B. T., McCleskey, M., et al. 2016, EPJA, 52, 1
Poppe, C. H., Anderson, J. D., Davis, J. C., Grimes, S. M., & Wong, C. 1976, PhRvC, 14, 438
Sbordone, L., Bonifacio, P., Caffau, E., et al. 2010, A&A, 522, 1
Sekharan, K., Laumer, H., Kern, B., & Gabbard, F. 1976, NucIM, 133, 253
Smith, M. S., Kawano, L. H., & Malaney, R. A. 1993, ApJS, 85, 219
Spitaleri, C., La Cognata, M., Lamia, L., Mukhamedzhanov, A. M., & Pizzone, R. G. 2016, EPJA, 52, 77
Tilley, D., Kelley, J., Godwin, J., et al. 2004, NuPhA, 745, 155
Tomandl, I., Vacík, J., Köster, U., et al. 2019, PhRvC, 99, 014612
Tribble, R. E., Bertulani, C. A., La Cognata, M., Mukhamedzhanov, A. M., & Spitaleri, C. 2014, RPPh, 77, 106901
Wang, M., Audi, G., Kondev, F. G., et al. 2017, ChPhC, 41, 030003
Yamaguchi, H., Kahl, D., & Kubono, S. 2020, Nucl. Phys. News, 30, 21
Yanagisawa, Y., Kubono, S., Teranishi, T., et al. 2005, NIMPA, 539, 74